Influence of Abradable Coating Wear Mechanical Properties on Rotor Stator Interaction

Alain Batailly, Mathias Legrand, Christophe Pierre

Influence des propriétés mécaniques du revêtement abradable sur l'interaction rotor/stator

Alain Batailly
Post-doctorant
Université McGill
Bâtiment d'ingénierie McDonald
Montréal H3A 2K6, Canada
alain.batailly@mcgill.ca

Mathias Legrand
Post-doctorant
Université McGill
Bâtiment d'ingénierie McDonald
Montréal H3A 2K6, Canada
mathias.legrand@mcgill.ca

Christophe Pierre
Professeur
Université McGill
Bâtiment d'ingénierie McDonald
Montréal H3A 2K6, Canada
christophe.pierre@mcgill.ca

Note: cet article a été publié dans sa version anglaise parmi les actes de la conférence ASME Turbo Expo 2011.
Note 2: un cours résumé de cet article est rédigé en français. Les figures et équations sont uniquement présentes dans la version anglaise.

RÉSUMÉ

L'optimisation des performances des turbomachines est en grande partie associée à la réduction des jeux entre parties fixes et tournantes de la structure. La

minimisation de ces jeux permet notamment de maximiser le taux de compression du fluide d'un étage à l'autre et a ainsi un effet significatif sur le rendement global de la turbomachine.

En contre-partie de la diminution des jeux de fonctionnement, les contacts entre les différents composants de la structures sont logiquement plus fréquents. Afin d'éviter des configurations pour lesquelles ces contacts pourraient s'avérer destructeurs, les concepteurs des turbomachines ont été amenés à considérer l'utilisation d'un revêtement abradable entre le sommet des aubes et le carter environnant. L'ajout de ce matériau permet de réduire les dégâts causés par des contacts directs aubes/carter et également d'ajuster les jeux de fonctionnement.

Cette étude a pour but d'évaluer l'influence des propriétés mécaniques du matériau abradable sur la simulation d'un cas de contact aube/abradable.

À partir d'un modèle éléments finis industriel 3D, une méthode de réduction modale (reposant sur la méthode de Craig-Bampton) permettant de prendre en compte les effets centrifuges appliqués sur l'aube est utilisée pour réduire les temps de calculs. Le carter, supposé parfaitement rigide, est ovalisé de façon à initier le contact puis les simulations temporelles sont effectuées en faisant varier la vitesse de rotation de l'aube ainsi que les propriétés mécaniques du matériau abradable.

Les résultats mettent en évidence la grande dépendance du niveau de vibration de l'aube aux propriétés mécaniques du revêtement abradable et notamment à son module d'Young. Contrairement à ce qu'une première approche intuitive pourrait laisser imaginer, les résultats présentés montrent que l'ajout d'un revêtement abradable n'est pas une condition suffisante pour diminuer l'amplitude des vibrations de l'aube.

Influence of abradable coating wear mechanical properties on rotor stator interaction

Alain Batailly
Postdoctoral fellows
McGill University
Bâtiment d'ingénierie McDonald
Montréal H3A 2K6, Canada
alain.batailly@mcgill.ca

Mathias Legrand
Postdoctoral fellows
McGill University
Bâtiment d'ingénierie McDonald
Montréal H3A 2K6, Canada
mathias.legrand@mcgill.ca

Christophe Pierre
Profesor
McGill University
Bâtiment d'ingénierie McDonald
Montréal H3A 2K6, Canada
christophe.pierre@mcgill.ca

ABSTRACT

In the field of turbomachines, better engine performances are achieved by reducing possible parasitic leakage flows through the closure of the clearance distance between blade tips and surrounding casings. Accordingly, direct contact is now commonly accepted as part of aircraft engines everyday life. In order to avoid possibly catastrophic scenarii due to high contact forces between the rotating and static components, implementation of abradable coatings has been widely recognized as a robust solution offering several advantages: reducing potential damage to the incurring blade as well as adjusting operating clearances,

in-situ, to accept physical contact events. In the present work, macroscopic behavior of the abradable coating is numerically approximated through a piecewise linear plastic constitutive law which allows for real time access to the current abradable layer profile. Contact simulations are carried out considering a three-dimensional industrial finite element model of a blade from a compressor stage and its surrounding casing, assumed perfectly rigid. Due to the large number of degrees of freedom, component mode synthesis methods are used. Simulations are repetitively carried-out over a wide rotational velocity range, and a large number of distinct values for two mechanical parameters of the abradable material are considered. Results show that the amplitude of vibration is highly sensitive to the Young modulus and the plastic modulus of the abradable and that a local maximum is detected. Also, a more realistic description of the contact forces allowing for a contribution in the tangential direction is suggested.

INTRODUCTION

Maximization of jet engine energy efficiency involves the reduction of parasitic leakage flows between blade-tips an surrounding casings onto which abradable coatings [1] are deposited.

The mechanical properties of the abradable material are of primary importance as it must preserve the incurring blade-tips from damage by being reasonably soft, but also be sufficiently hard to stand very high temperatures and high-speed gas flows with inherent solid particles [2]. It has been detected by experimental investigations that erosive wear of abradable coatings may play a significant role in the initiation of divergent behaviors[1] such as propagating cracks in blade roots [3]. Accordingly, it seems urgent to enrich the limited current knowledge of the circumstances under which they occur [4].

[1] a divergent behavior is here observed when the amplitude of vibration continuously grows with time.

It is here assumed that plasticity with its inherent abilities to represent permanent deformation in a simple fashion stands as a natural first macroscopic approach in order to account for abradable coatings erosive wear. Even though mass removal is neglected and the exact dynamics of the abradable material are not modeled, it is thought that the behavior of the blade will be properly predicted. Furthermore, the energy transferred from the blade to the casing during contact interaction is partially dissipated because of wear: this can be captured by a plastic constitutive law. Based on [5][2], the plastic constitutive law is enriched in order to allow for a more realistic description of contact forces on the blade tip.

As described in [5], the proposed numerical tool embeds in an explicit time marching technique, a contact detection procedure together with the calculation of internal forces and plastic deformations arising in the abradable material, thus controlling the desired amount of wear. It allows for real time access to the current profile of the abradable, supposedly key feature for detecting such critical behaviors mentioned above.

STRUCTURAL MODEL AND EQUATIONS OF MOTION

Finite element model

The present study deals with a single rotating blade as well as the corresponding surrounding casing both from a low pressure compressor stage, as depicted in Fig. 1. Within the well-known finite element framework under the assumption of small displacements, vector $\mathbf{u}$ stores all the displacement degrees-of-freedom of the blade and the respective mass matrix $\mathbf{M}$, damping matrix $\mathbf{D}$, stiffness matrix $\mathbf{K}$ and contact forces $\mathbf{F}^c$ are built accordingly. The resulting gov-

[2]This article is also available online at http://hal.archives-ouvertes.fr/hal-00413728/fr It may be useful to the reader because it contains most of the theoretical tools and numerical developments used in the present paper.

erning equations of motion take the form:

$$\mathbf{M\ddot{u}} + \mathbf{D\dot{u}} + \mathbf{Ku} + \mathbf{F}^{c} = \mathbf{0} \tag{1}$$

complemented with the usual contact constraints detailed later in the paper. Thorough preliminary simulations have shown that the casing remains insen-

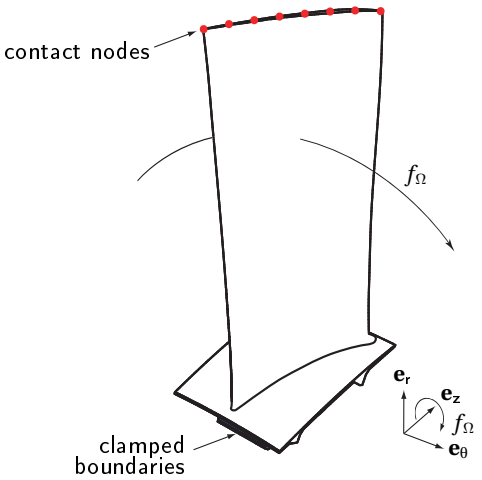

Figure 1: BLADE UNDER INVESTIGATION WITH FIXED DISPLACEMENT BOUNDARY CONDITIONS AND EIGHT INTERFACE NODES UNDERGOING CONTACT CONSTRAINTS

sitive to the contact interaction with the blade and is not modeled as a flexible component.

Reduced-order model and component mode synthesis

The introduced finite element model of the blade is numerically too large and leads to cumbersome computation times. It is reduced based on the Craig-Bampton procedure [6] and combined to the theoretical developments of [7] in order to obtain a reduced-order model taking into account centrifugal stiffening.

It is shown in [7] that the stiffness matrix $\mathbf{K}$ of the rotating structure may be written as a polynomial expansion over a specific rotational frequency range $f_\Omega \in [0;\ f_{\Omega,\mathrm{m}}]$ such as:

$$\mathbf{K}(f_\Omega) = \mathbf{K}^0 + f_\Omega^2 \mathbf{K}^1 + f_\Omega^4 \mathbf{K}^2 \tag{2}$$

where:

$$\begin{aligned} \mathbf{K}^0 &= \mathbf{K}(0) \\ \mathbf{K}^1 &= \frac{1}{3f_{\Omega,\mathrm{m}}^2}\left[16\mathbf{K}\left(\frac{f_{\Omega,\mathrm{m}}}{2}\right) - \mathbf{K}(f_{\Omega,\mathrm{m}}) - 15\mathbf{K}(0)\right] \\ \mathbf{K}^2 &= \frac{3}{4f_{\Omega,\mathrm{m}}^4}\left[\mathbf{K}(f_{\Omega,\mathrm{m}}) - 4\mathbf{K}\left(\frac{f_{\Omega,\mathrm{m}}}{2}\right) + 3\mathbf{K}(0)\right] \end{aligned} \tag{3}$$

Computation of the reduced order model using the Craig-Bampton CMS method is then carried out using three modal reduction bases calculated for $f_\Omega = 0$, $f_\Omega = f_{\Omega,\mathrm{m}}/2$ and $f_\Omega = f_{\Omega,\mathrm{m}}$ which yields the following final transformation matrix $\mathbf{\Phi}$:

$$\mathbf{\Phi} = \begin{bmatrix} \mathbf{I} & \mathbf{0} & \mathbf{0} & \mathbf{0} & \mathbf{0} & \mathbf{0} \\ \mathbf{\Phi}_\mathrm{R}(0) & \mathbf{\Phi}_\mathrm{R}\left(\frac{f_{\Omega,\mathrm{m}}}{2}\right)^* & \mathbf{\Phi}_\mathrm{R}(f_{\Omega,\mathrm{m}})^* & \mathbf{\Phi}_\mathrm{L}(0) & \mathbf{\Phi}_\mathrm{L}\left(\frac{f_{\Omega,\mathrm{m}}}{2}\right) & \mathbf{\Phi}_\mathrm{L}(f_{\Omega,\mathrm{m}}) \end{bmatrix} \tag{4}$$

where matrices $\mathbf{\Phi}_\mathrm{R}(f_\Omega)$ and $\mathbf{\Phi}_\mathrm{L}(f_\Omega)$ respectively stand for the n_c[3] constraint modes and the η fixed-interface modes computed at f_Ω. Superscript * indicates that matrix $\mathbf{\Phi}_\mathrm{R}(0)$ was subtracted: $\mathbf{A}^* = \mathbf{A} - \mathbf{\Phi}_\mathrm{R}(0)$. Equation (4) may be written, after orthonormalization of the selected constraint and fixed-interface modes, as:

$$\mathbf{\Phi} = \begin{bmatrix} \mathbf{I} & \mathbf{0} \\ \mathbf{\Phi}_\mathrm{R}(0) & \mathbf{\Psi} \end{bmatrix} \tag{5}$$

and thus defines the projection used to reduce the size of the system:

$$\mathbf{u} = \begin{pmatrix} \mathbf{u}_\mathrm{f} \\ \mathbf{u}_\mathrm{i} \end{pmatrix} = \begin{bmatrix} \mathbf{I} & \mathbf{0} \\ \mathbf{\Phi}_\mathrm{R}(0) & \mathbf{\Psi} \end{bmatrix} \begin{pmatrix} \mathbf{u}_\mathrm{f} \\ \mathbf{q} \end{pmatrix} \tag{6}$$

where the size of the reduced displacement vector $(\mathbf{u}_\mathrm{f}\ \mathbf{q})^\mathrm{T}$ is substantially smaller than the size of the physical displacement vector $(\mathbf{u}_\mathrm{f}\ \mathbf{u}_\mathrm{i})^\mathrm{T}$.

[3] n_c corresponds to the number of DoF defining the contact interface on the tip of the blade.

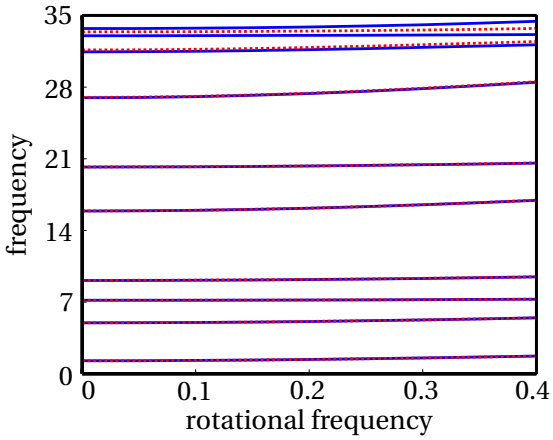

Figure 2: CAMPBELL DIAGRAM OF THE REDUCED-ORDER MODEL (– –) AND THE FINITE ELEMENT MODEL (——) BOTH INCLUDING CENTRIFUGAL STIFFENING

The dynamics of the considered blade is now seen as a full set of constraint modes whose contributions $\mathbf{u}_\mathrm{f}$ are the physical displacements of the interface DoF, complemented with a set of fixed-interface modes of contribution $\mathbf{q}$ that control the precision of the numerical simulations. As deduced from Eq. (6), the contact constraints can directly be treated in the reduced space if the anticipated contact locations are defined as interface nodes, thus avoiding permanent forward and backward mappings to the physical space. This is a major feature motivating the choice of the Craig-Bampton technique.

In this study, eight nodes (from the leading edge to the trailing edge as displayed in Fig. 1) define the contact interface. The maximum[4] dimension n of the subsequent reduced-order model is $n = 3\eta + 3n_\mathrm{c}$. In order to ensure modal convergence, six fixed-interface modes are required at each rotational frequency and the final size of the blade model after reduction is 85 DoF. In order to illustrate the quality of the computed reduced-order model, a superimposition of both its Campbell diagram and the Campbell diagram of the as-

[4]The orthonormalization of Eq. (4) may lead to a reduction of the rank of the projection matrix $\mathbf{\Phi}$

sociated finite element model are plot in Fig. 2. For confidentiality reasons, frequencies in Fig. 2 are normalized with respect to the first eigenfrequency of the structure at rest, *i.e.* $f_\Omega = 0$. It is shown that the reduced-order model allows to accurately predict the first seven eigenfrequencies with respect to the rotational frequency.

Eq. (1) has undergone the projection defined in Eq. (6) so that the dimension of the system is now reduced. However, for the sake of simplicty, notations are not modified. Moreover, since the chosen Craig-Bampton interface nodes of the blade, as such, do not contain any information about the *true* geometry of the blade tip, this has to be numerically included in the solution method, as illustrated in Fig. 3, in order to ensure space convergence of the worn pattern.

CONTACT DYNAMICS

In order to properly define the notations later used in the proposed algorithm, derivation of the equations is conducted in the context of contact mechanics [8, 9] even though contact forces exerting between blade interface nodes and facing abradable coatings will not be computed explicitly.

By choice, the blade supports the master surface Γ_c^m from which the abradable coating can be parameterized. It is then possible to find for any material point $\mathbf{x} \in \Gamma_c^m$, limited here to the interface nodes[5], its closest counterpart $\bar{\mathbf{y}}$ on the abradable material slave surface Γ_c^s:

$$\bar{\mathbf{y}} = \arg\min_{\mathbf{y}\in\Gamma_c^s} \|\mathbf{x}-\mathbf{y}\| \tag{7}$$

According to these notations, the discretized clearance between the two components can be stated:

$$\mathbf{g}(\mathbf{x}) = \mathbf{g}_0(\mathbf{x}) + \left(\mathbf{u}^m(\mathbf{x}) - \mathbf{u}^s(\bar{\mathbf{y}}(\mathbf{x}))\right)\cdot\mathbf{n} \tag{8}$$

[5]In other words, $\mathbf{x}$ is here limited to a known set of interface DoF and can be seen as a set of fixed indices.

where $\mathbf{g}_0(\mathbf{x})$ represents the initial positive gap and $\mathbf{n}$, the outward normal to Γ_c^s. The contact conditions, referred to as the Kuhn-Tucker optimality conditions, considered in a vector-compact form[6], are such that for all $\mathbf{x} \in \Gamma_c^m$:

$$\mathbf{t}_N \geqslant 0, \ \ \mathbf{g}(\mathbf{x}) \geqslant 0, \ \ \mathbf{t}_N \mathbf{g}(\mathbf{x}) = 0 \tag{9}$$

where $\mathbf{t}_N$ stands for the discretized contact pressure, assumed positive and acting on the contact interface. The initial clearances go from $1.5 \cdot 10^{-2}$% to $4.3 \cdot 10^{-2}$% of the blade length.

ABRADABLE CONSTITUTIVE LAW WITH PLASTICITY

As a first approach, the abradable coating is discretized with the usual one-dimensional two-node bar elements, as displayed in Fig. 3, undergoing a non-linear plastic constitutive law. For the sake of clarity, the curvature of the casing is not represented on this figure while it is taken into account in the simulations. Clearance closure due to tangential vibration of the blade is also considered. The details of this abradable constitutive law depicted in Fig. 4 is given

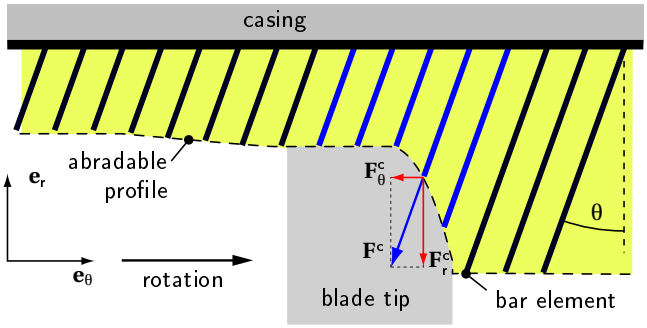

Figure 3: BLADE INTERFACE NODE NUMERICAL PROFILE.

in [5] and are summarized here for clarity. Three parameters are considered: the Young modulus E, the plastic modulus K and the elastic limit σ_Y.

[6]These conditions written in a vector form have to be read coordinate by coordinate for each interface DoF where contact is treated.

A single element is used over the thickness of the abradable layer since calculations are performed in a quasi-static compression framework only. A noticeable difference with the description given in [5] concerns parameter θ which controls the rotated position of the abradable elements with respect to the radial direction. Through this parameter, the contact effort $\mathbf{F}^c$ exerting on

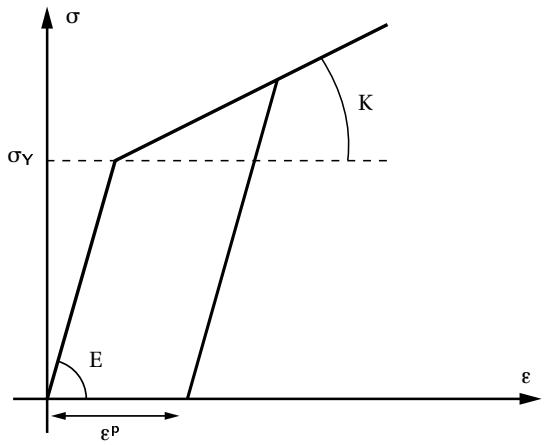

Figure 4: DEFINITION OF THE PLASTICITY CONSTITUTIVE LAW OF THE ABRADABLE COATING.

the blade tip may now have both a tangential $\mathbf{F}^c_\theta$ and a radial $\mathbf{F}^c_r$ contribution with $\mathbf{F}^c_\theta = -\sin(\theta)\|\mathbf{F}^c\|\mathbf{e}_\theta$ and $\mathbf{F}^c_r = -\cos(\theta)\|\mathbf{F}^c\|\mathbf{e}_r$. The existence of the tangential component $\mathbf{F}^c_\theta$ is conditioned by $\theta > 0$.

Over the circumference of the casing, 2,000 abradable elements are used. Also, all the results and material properties (frequencies, amplitudes, Young modulus E, plastic modulus K and elastic limit σ_Y) are normalized. In particular, frequencies have been normalized with respect to the first eigenfrequency of the blade at rest.

CASE STUDY

Previous simulations of blade-tip/casing contact interactions featured an ovalized casing. As a matter of fact, it has been experimentally observed that thermal loading on the casing due to a temperature gradient in the turbomachine leads to an ovalization. However, the shape of the contact surface of the casing at rest may not be perfectly circular. In order to take into account these imper-

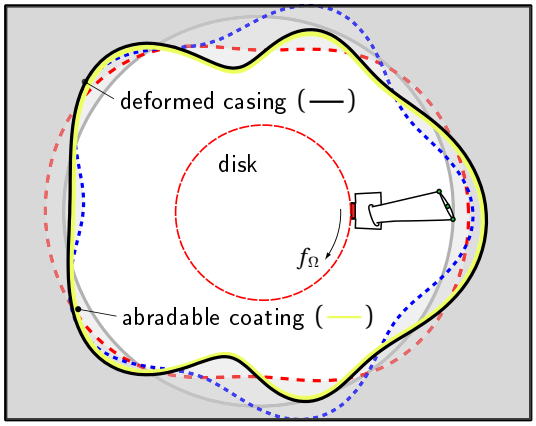

Figure 5: CASING INITIAL INNER SHAPE (—), 2-NODAL DIAMETER (– –), 5-NODAL DIAMETER (– –), AND COMBINATION OF 2 AND 5-NODAL DIAMETER DISTORSION (—).

fections, the casing is here distorted along both a 2 and a 5-nodal diameter free vibration mode, as depicted in Fig. 5[7].

Simulations parameters of the abradable coating are chosen as follows: $E = 11$, $K = 0.5$, $\sigma_Y = 1.5 \cdot 10^{-8}$ and several simulations are launched over the operating rotational frequency range of the blade $f_\Omega \in [0;\ 0.4]$. In this example, the abradable elements are straight and $\theta = 0$ rad. For each rotational frequency, the blade performs exactly twenty revolutions and attention is given to the abradable coating wear level at the end of the simulation, as depicted in

[7]The deformation of the casing pictured in Fig. 5 is magnified. The actual deformation of the casing leads to a maximum radial displacement of one millimeter.

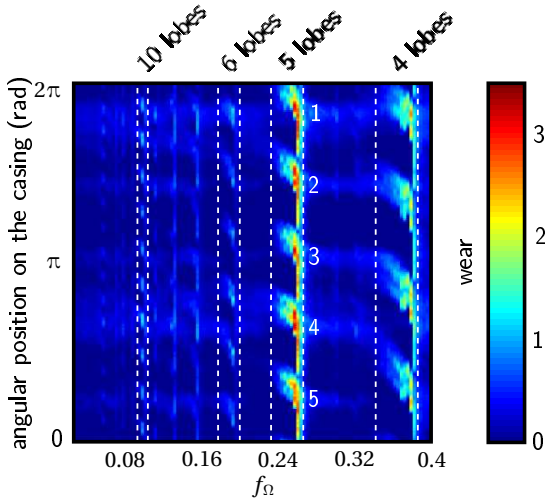

Figure 6: ABRADABLE COATING WEAR PATTERNS.

Fig. 6. Consequently, each vertical line of Fig. 6 represents a different simulation.

Due to the shape of the casing, there are five privileged contact areas along the casing. Accordingly, five worn lobes on the abradable coating may be usually observed: this is illustrated in Fig. 6 for $f_\Omega \in [0;\ 0.08]$ and $f_\Omega \in [0.24;\ 0.34]$. However, for specific rotational frequencies, a different number of lobes may be detected. As an example, it is highlighted in Fig. 6 that $f_\Omega \simeq 0.1$ yields a ten-lobe profile.

In addition to the wear patterns pictured in Fig. 6, it may be of great interest to plot the corresponding blade displacements in the frequency domain. Accordingly, for each rotational frequency, a Fourier transform of the radial vibration of the first contact node of the blade located in the leading edge is performed on the steady state portion of the response, *i.e.* over the last ten revolutions of the blade. The final spectrum of the blade response is depicted in Fig. 7. Beside the spectrum, one may notice the increase of the first eigenfrequency of the blade with the rotational frequency. In the following, this line will be referred to as C_1. Furthermore, straight lines $f = k f_\Omega$ in the $(f;\ f_\Omega)$ plane show engine orders of order k, and are denoted $eo(k)$ in the sequel.

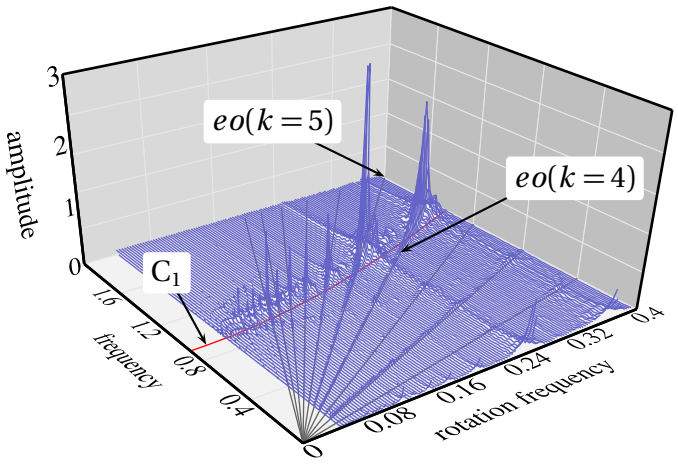

Figure 7: SPECTRUM OF THE BLADE RESPONSE VERSUS f_Ω (—); FIRST EIGENFREQUENCY OF THE BLADE (—).

The spectrum plot in Fig. 7 allows for a better understanding of the wear map. Indeed, the maximum wear levels detected for $f_\Omega \simeq 0.26$ (five lobes) and $f_\Omega \simeq 0.38$ (four lobes) match two maxima of amplitude of vibration of the blade. These maxima respectively occur at the intersection of $eo(5)$ with C_1 and $eo(4)$ with C_1 in agreement with the number of observed lobes.

RESULTS

The system of interest is highly nonlinear and its resonances are strongly dependant on parameters such as rotational frequency and material properties of the abradable material. The point of this section is to better understand the role of abradable coating in the interactions that may arise from blade-tip/casing contact.

Mechanical properties of the abradable coating

The results are presented for $\theta = 0$ rad which means that the abradable elements are oriented along the radial direction. Focus is given to the sensitivity of the amplitude of vibration of the blade during interaction to the Young modulus E and the plastic modulus K. The casing is deformed along a two-nodal diameter free vibration mode only so that there are two privileged contact areas on the casing together with the respective contact stimulations of the blade. Each simulation comprises 20 full revolutions of the blade.

Young modulus sensitivity

For each Young modulus ($E_{min} = 0.11;\ 0.2;\ 0.5;\ 1.1;\ 1.5;\ 2;\ 5\ ;\ 11;\ E_{max} = 20$) of the abradable material, results are analyzed in the frequency domain. Figure. 8 pictures the results for $E = 0.11$. Two vibratory maxima clearly arise for

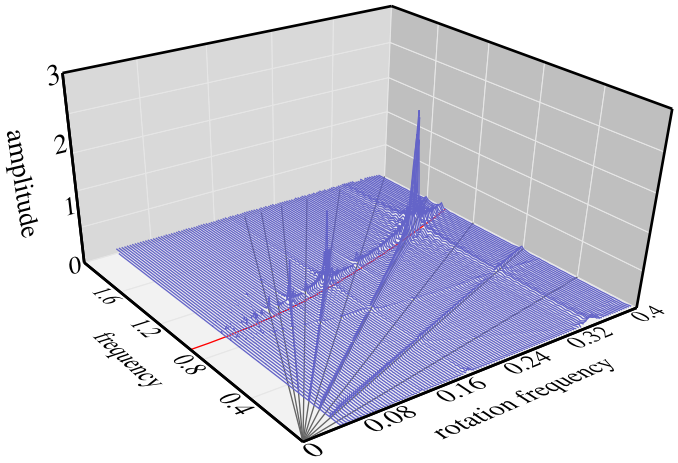

Figure 8: SPECTRUM OF THE BLADE RESPONSE FOR E = 0.11.

$f_\Omega = 0.21$ and $f_\Omega = 0.31$ respectively corresponding to the intersections of $eo(4)$ and $eo(6)$ with C_1. Larger amplitudes of vibration lie either on $eo(k)$ lines with k even either on C_1. Also, no significant amplitude could be observed along $eo(k)$

lines with k odd. We assume that these observations are consistent with the contact configuration: because there are two symmetric privileged contact areas, the blade is preferably excited along an even super-harmonic of the engine-order.

Accordingly, all the presented results strongly depend on the adopted scenario of interaction, and further investigations have to be conducted to better understand the mechanisms of wear and subsequent possible mechanical failure. For E = 1.1, the vibration of the blade is significantly modified as shown

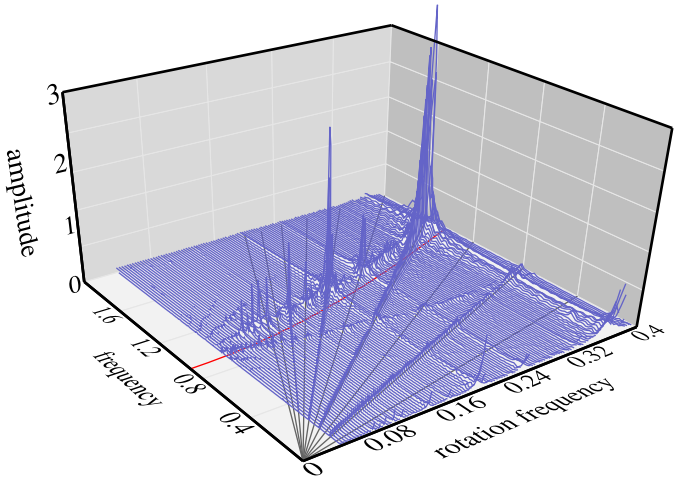

Figure 9: BLADE RESPONSE SPECTRUM FOR E = 1.1.

in Fig. 9. Maxima of amplitude are higher than for E = 0.11 and significant amplitudes of vibration appear at the intersection of each engine order $eo(k)$ with C_1. The sensitivity of the results to the Young and plastic modulii is observed locally, focusing on the evolution of the maxima detected at the intersection of $eo(4)$ and $eo(6)$ with C_1.

Local maxima evolution.

Figure 10 highlights two maximum of amplitude for $k = 6$ and for $k = 4$. The focus is made on the evolution of the amplitude of each maximum (respectively

Y6 and Y4) as well as on the rotational frequency for which they appear (respectively f6 and f4).

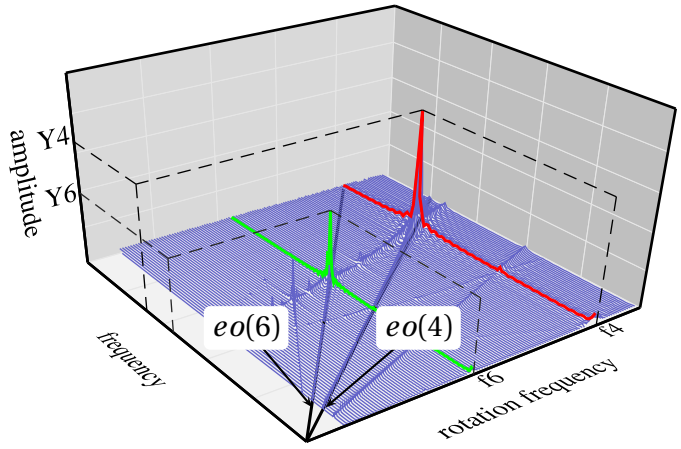

Figure 10: BLADE RESPONSE SPECTRUM FOR E = 0.11 AND K = 0.5, MAXIMUM FOR $k = 4$ (—), AND $k = 6$ (—).

In agreement with the notations of Fig. 10, results will consist in Y4(E,K), Y6(E,K), $f4$(E,K) and $f6$(E,K). Y4 and f4 are plotted as histograms in Fig. 11, and 12, respectively. As it could have been expected, there is no simple linear relationship between Y4 or f4 and the Young and plastic modulii. If the Young modulus is too low ($E < E_{min}$), the abradable is too soft to yield a dangerous interaction, while if the Young modulus is too high ($E > E_{max}$), the contact configuration will be equivalent to direct contact between the blade-tip and the rigid casing.

Concerning amplitude Y4, a maximum may be identified for (E,K) = (1.1; 0.5)[8]. This is a very important result showing that abradable coating may actually increase the amplitude of vibrations of the blade. In that case, Fig. 11 underlines that the amplitude of vibration of the blade for any K is the highest for E = 1.1.

[8]One may notice that other values of E and K lead to very high amplitudes such as (E,K) = (1.1; 5), (E,K) = (0.5; 0.5) or (E,K) = (1.5; 1).

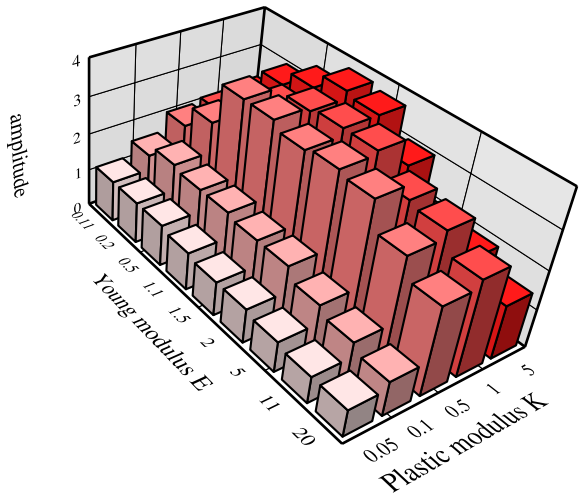

Figure 11: Y4 VERSUS E AND K.

Results pictured in Fig. 12 for f4 underline the role of the plastic modulus in the process of *contact stiffening*[9]. If the Young modulus is not too low ($E > 0.5$), f4 increases with the plastic modulus. In other words, the maximum of amplitude on the spectrum is shifted to higher frequencies when the plastic modulus increases.

Also, it appears that the sensitivity of both Y4 and f4 regarding to the Young modulus is highly dependant on the plastic coefficient: if $K \leqslant 0.1$, Y4 and f4 do not significantly vary with E.

Results for Y6 and f6 are depicted in Fig. 13 and 14. Variations of Y6 and f6 with respect to the Young and the plastic modulii are comparable with the results obtained for Y4 and f4, respectively. The maximum of vibration identified in Fig. 11 for Y4 may be more clearly identified in Fig. 13 for Y6 and also occurs for $(E,K) = (1.1;\ 0.5)$.

These results highlight the fact that material properties of the abradable ma-

[9]Contact stiffening consists in an increase of the natural frequencies of the system due to contact.

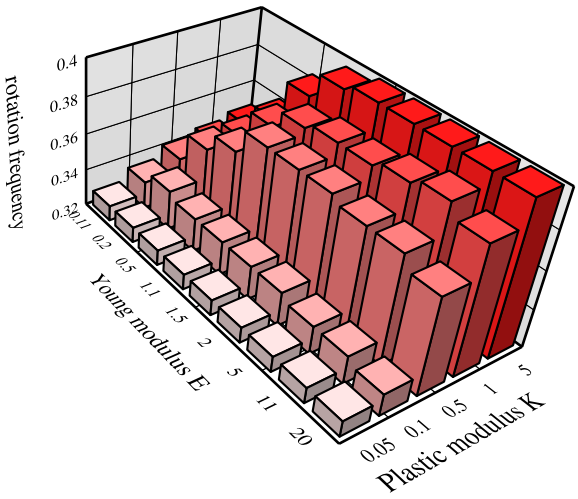

Figure 12: f4 VERSUS E AND K.

terial must be chosen carefully. Indeed, it is emphasized that abradable coating does not always reduce the amplitude of vibration of a blade, but may cause an increase for specific plastic and Young modulii which could be demonstrated with our model.

Influence of parameter θ

Results now feature a non-zero θ parameter as illustrated in Fig. 3. As suggested by experimental observations [10], the ratio between tangential and radial component is close to $\mu = 0.15$. The tangential component of contact effort may be seen as the resistance to abradable removal. Accordingly, the θ parameter is chosen so that $\sin(\theta) \simeq 0.15$ and $\theta = 0.15$ rad. The Young modulus is $E = 2$ and the plastic modulus is $K = 0.5$. The blade response spectra for $\theta = 0$ rad and $\theta = 0.15$ rad are depicted in Fig. 15 and 16, respectively. These spectra are similar to the ones detailed in the previous sections, they also feature the C_1 and $eo(k)$ lines mentioned in Fig. 8.

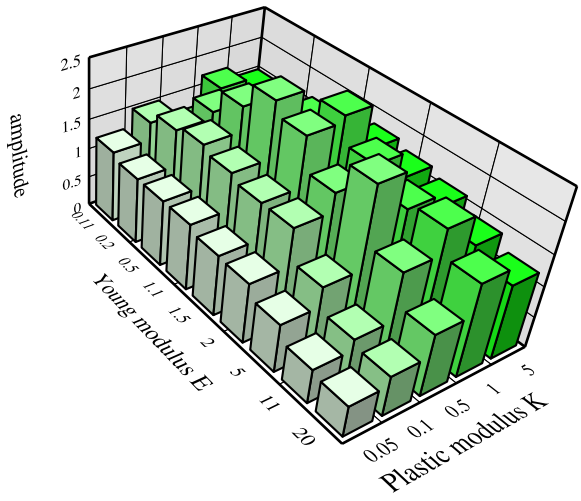

Figure 13: Y6 VERSUS E AND K.

Results show that the introduction of the tangential component of the contact force tends to reduce the amplitude of vibration of the blade. One may observe that when $\theta = 0.15$ rad, the maxima of amplitude of vibration (mostly the intersections of C_1 and $eo(k)$ lines) occur at lower rotational frequencies than for $\theta = 0$ rad. These results are consistent with a global softening of the contact case due to a loosen constrained contact configuration. Results in the time domain for specific rotational frequencies underline the sensitivity to θ. The second maximum vibrational amplitude of the blade is detected for a rotational frequency $f_\Omega = 0.19$ when $\theta = 0.15$ rad and for $f_\Omega = 0.197$ when $\theta = 0$ rad. Vibration of the radial displacement of the first contact node of the blade for both these frequencies are respectively pictured in Fig. 17 and in Fig. 18. These two figures show that while a divergent behavior is detected at $f_\Omega = 0.19$ with $\theta = 0.15$ rad, the same simulation with $\theta = 0$ rad leads to a non-divergent motion with constant vibration of the blade. Symmetrically, a divergent behavior is detected at $f_\Omega = 0.197$ with $\theta = 0$ rad and the same simulation with $\theta = 0.15$ rad leads to a non divergent motion. The observation of wear level — depicted in

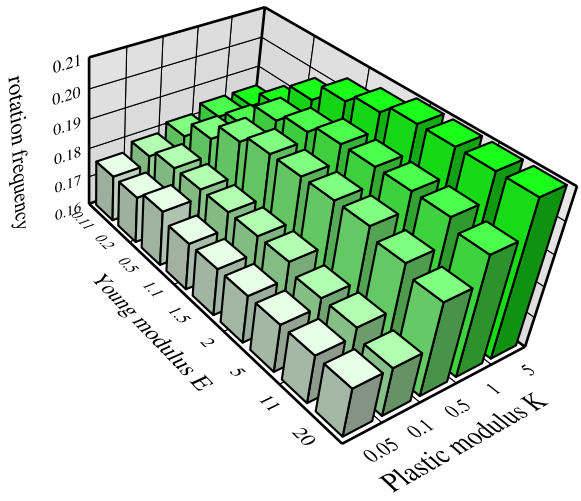

Figure 14: f6 VERSUS E AND K.

Figs. 19(a) and 19(b) — of the abradable coating underlines the differences between the simulations launched for $\theta = 0$ rad and $\theta = 0.15$ rad. One may notice that the divergent behavior observed for $f_\Omega = 0.19$ and $\theta = 0.15$ rad is similar to the one observed for $f_\Omega = 0.197$ and $\theta = 0$ rad since they both lead to a 6-lobe wear profile. Consequently, the resistance to abradable removal – represented by the tangential component of the contact effort – appears as a non-negligible phenomenon. Its role in the softening of the contact case has been highlighted. Further work is required to assess the role of this tangential component in the sollicitation of the bending modes of the blade.

CONCLUSION

A macroscopic plastic constitutive law approximating the abradable coating removal proved to be a very efficient way to enrich rotor/stator contact simulations at reasonable computational cost. In addition to this law, reduced-order

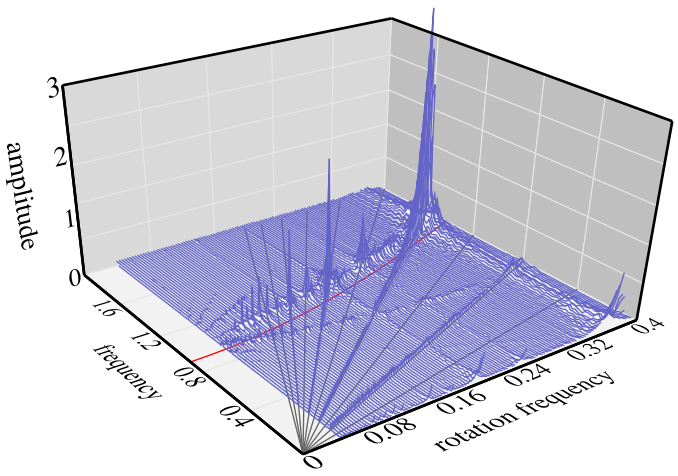

Figure 15: SPECTRUM OF THE BLADE RESPONSE FOR $\theta = 0$ rad.

models taking into account centrifugal stiffening and more realistic clearance closure are used in this study.

First results show that mechanical properties of the abradable material significantly influence the amplitude of vibration of the blade during interaction. More important is the fact that while the Young and plastic modulii of the abradable model vary, a maximum vibrational amplitude of the blade is identified. Accordingly, the introduced macroscopic model suggests abradable coatings – with specific material properties – may lead to unexpected higher level of vibrations than a direct blade/casing contact case.

The second part of this study is dedicated to an improvement of the plastic constitutive law that allows for a more realistic description of the contact forces on the tip of the blade. It is shown that the existence of a tangential contribution in the contact forces slightly shifts the interaction motion toward lower rotational frequencies and accordingly, the interaction rotational frequencies tend to decrease.

Work is in progress to calibrate the material properties of an abradable material on simpler contact cases with a comparison of numerical results and ex-

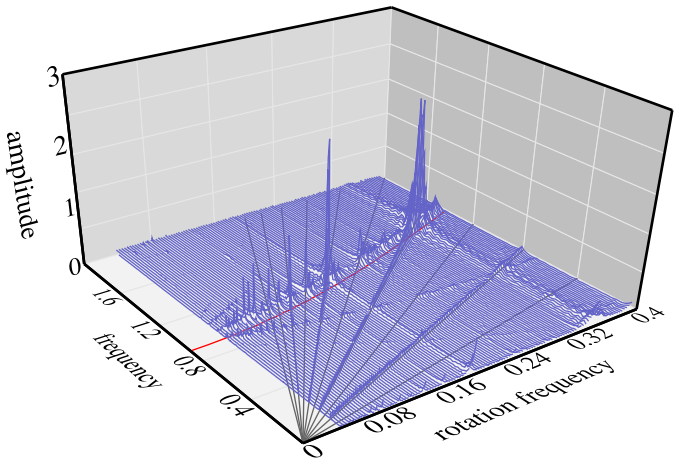

Figure 16: BLADE RESPONSE SPECTRUM FOR $\theta = 0.15$ RAD.

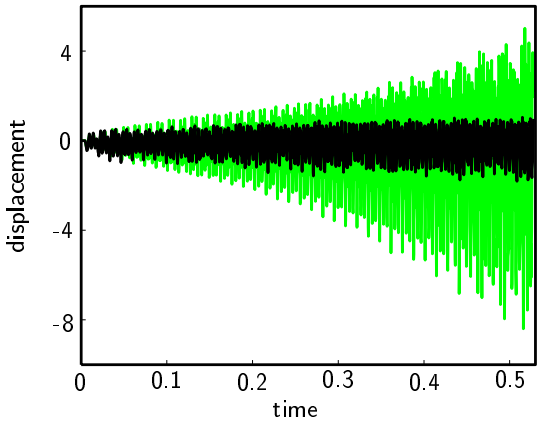

Figure 17: RADIAL DISPLACEMENT OF THE FIRST CONTACT NODE OF THE BLADE AT $f_\Omega = 0.190$ FOR $\theta = 0$ RAD (—) AND $\theta = 0.15$ RAD (—).

perimental data.

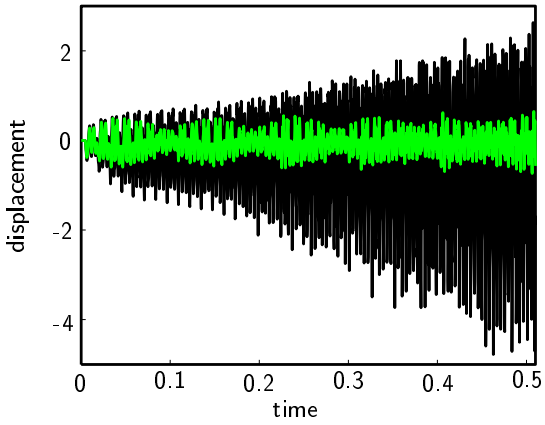

Figure 18: RADIAL DISPLACEMENT OF THE FIRST CONTACT NODE OF THE BLADE AT $f_\Omega = 0.197$ FOR $\theta = 0$ RAD (—), AND $\theta = 0.15$ RAD (—).

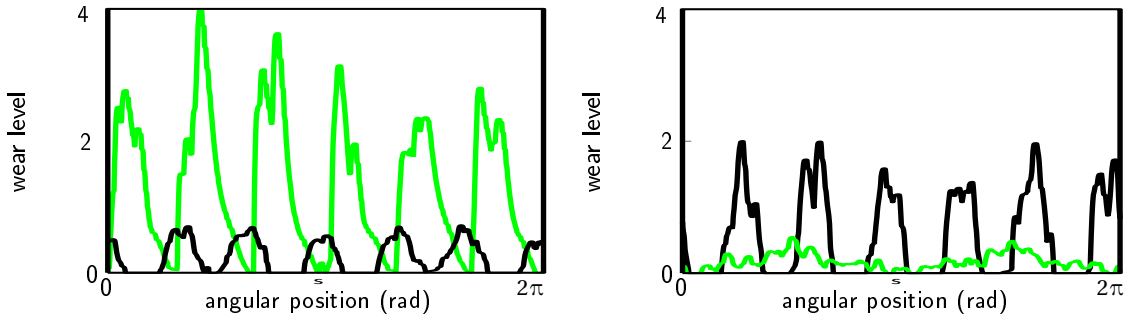

(a) $f_\Omega = 0.190$.

(b) $f_\Omega = 0.197$.

Figure 19: WEAR LEVEL OF THE ABRADABLE COATING FOR $\theta = 0$ RAD (—), AND $\theta = 0.15$ RAD (—).

ACKNOWLEDGEMENT

Thanks go to Snecma for its technical and financial support. This work takes place in the framework of the MAIA mechanical research and technology program sponsored by CNRS, ONERA and SAFRAN Group.

NOMENCLATURE

$\mathbf{D}$	Damping matrix
$\mathbf{g}$	Gap function
$\mathbf{K}$	Stiffness matrix
$\mathbf{M}$	Mass matrix
$\mathbf{q}$	Modal DoF
$\mathbf{t}_N$	Contact pressure
$\mathbf{u}$	Physical DoF
$\mathbf{u}_f$	Contact DoF
$\mathbf{u}_i$	Internal DoF
$\mathbf{\Phi}$	Transformation matrix
$\mathbf{\Phi}_L$	Fixed-interface modes
$\mathbf{\Phi}_R$	Constraint modes
$\mathbf{F}^c$	Contact forces
$\mathbf{F}^c_r$	Radial component of $\mathbf{F}^c$
$\mathbf{F}^c_\theta$	Tangential component of $\mathbf{F}^c$
μ	Ration between the norms of tangential and radial contact forces
σ	Stress
σ_Y	Elastic limit
θ	Angle of rotation of the abradable elements

ε	Plastic strain
ε	Strain
E	Young modulus
f	Frequency
f_Ω	Rotational frequency of the blade
$f_{\Omega,\mathrm{m}}$	Maximum rotational frequency of the blade
h	Time step
K	Plastic modulus

References

[1] M. Yi, J. He, B. Huang, and H. Zhou. Friction and wear behaviour and abradability of abradable seal coating. *Wear*, 231(1):47 – 53, 1999. ISSN 0043-1648. doi: 10.1016/S0043-1648(99)00093-9.

[2] X. Ma and A. Matthews. Investigation of abradable seal coating performance using scratch testing. *Surface and Coatings Technology*, 202(4-7): 1214 – 1220, 2007. ISSN 0257-8972. doi: 10.1016/j.surfcoat.2007.07.076.

[3] C. Padova, J. Barton, M. Dunn, and S. Manwaring. Experimental results from controlled blade tip/shroud rubs at engine speed. *Journal of Turbomachinery*, 129(4):713–723, 2007. doi: 10.1115/1.2720869.

[4] J. Jiang, J. Ahrens, H. Ulbrich, and E. Scheideler. Contact model of a rotating rubbing blade. In *Proceedings of the 5th International Conference on Rotor Dynamics of the IFTOMM*, pages 478 – 489, Darmstadt, Germany, June 1998.

[5] M. Legrand and C. Pierre. Numerical investigation of abradable coating wear through plastic constitutive law: Application to aircraft engines. In *Proceedings of the ASME IDETC/CIE - DETC2009-87669*, San Diego, USA, September 2009.

[6] R.R. Craig and C.C. Bampton. Coupling of substructures for dynamics analyses. *AIAA Journal*, 6(7):1313 – 1319, 1968. doi: 10.2514/3.4741.

[7] A. Sternchüss and E. Balmès. On the reduction of quasi-cyclic disks with variable rotation speeds. *Proceedings of the International Conference on Advanced Acoustics and Vibration Engineering (ISMA)*, pages 3925–3939, 2006.

[8] T. Laursen. *Computational contact and impact mechanics - Fundamentals of modeling interfacial phenomena in nonlinear finite element analysis*. Springer-Verlag, Heidelberg, 2002. ISBN 3540429069.

[9] P. Wriggers. *Computational contact mechanics*. Wiley, 2002. ISBN 3540326081.

[10] C. Padova, J. Barton, M.G. Dunn, S. Manwaring, G. Young, M.Jr. Adams, and M. Adams. Development of an experimental capability to produce controlled blade tip/shroud rubs at engine speed. *Journal of Turbomachinery*, 127:726–735, 2005.